APPLIED SCIENCES AND ENGINEERING

FAP-catalyzed in situ self-assembly of magnetic resonance imaging probe for early and precise staging of liver fibrosis

Zhuoyao Wu†, Weiwei Zeng†, Weitao Yang†, Jinyan Yi, Dinghua Liu, Yan Xu, Chang Liu, Kexin Bian, Hui Wang, Bingbo Zhang*

Liver fibrosis is an inevitable stage in the progression of most chronic liver diseases. Early diagnosis and treatment of liver fibrosis are crucial for effectively managing chronic liver conditions. However, there lacks a noninvasive and sensitive imaging method capable of early assessing fibrosis activity. Here, we report a molecular magnetic resonance imaging (MRI) probe for imaging fibroblast activation protein (FAP), which is overexpressed on activated hepatic stellate cells (HSCs) even in very early fibrotic livers. This method relies on FAP-catalyzed in situ self-assembly of its substrate probe that leads to the increase of the rotational correlation time (τ_R) of probe, thereby notably amplifies T_1 MRI signal. Thanks to the superior specificity and efficiency of enzymatic reaction, our method has been validated as highly selective and sensitive to FAP in two liver fibrosis mouse models. By establishing a direct correlation between MRI signals and fibrosis activity, our method enables continuous monitoring of liver fibrotic disease progression and assessment of treatment responses.

INTRODUCTION

Chronic liver disease is a major global health issue, affecting 1.3 billion people and causing 2 million deaths yearly (*1*, *2*). Liver fibrosis, a pathological repair response to various chronic injuries, involves the abnormal proliferation of intrahepatic connective tissue caused by diverse pathogenic factors (*3*, *4*). It is a critical pathological process in the progression of chronic liver disease to cirrhosis and liver failure; liver fibrosis can be reversed if detected and treated early, greatly affecting prognosis (*5*). Therefore, accurate and early diagnosis of liver fibrosis is crucial for timely intervention, prevention of cirrhosis and liver cancer, and guiding the assessment of therapeutic efficacy and prognosis.

Clinically, liver biopsy has been the "gold standard" for assessing liver fibrosis staging, but it is invasive and can cause discomfort, pain, infection, and other complications, leading to poor patient compliance (*6*). In addition, the limited biopsy sites can result in sampling errors, hindering dynamic observation and follow-up (*7*, *8*). Serum biomarker testing for liver fibrosis offers advantages such as simplicity and repeatability, but its diagnostic sensitivity and specificity are insufficient due to factors like autoimmunity and metabolism (*9*). Medical imaging, with its ability to achieve noninvasive and dynamic disease diagnosis, plays a crucial role in anatomical structure visualization, molecular visualization, and therapeutic response assessment (*10*, *11*). Among various imaging techniques, magnetic resonance imaging (MRI) stands out due to its advantages such as nonradiation, high tissue penetration depth, and good spatial resolution (*12*–*15*). In recent years, MRI has provided new approaches for the noninvasive assessment of liver fibrosis, using techniques such as native T_1 mapping (without contrast agents) (*16*), T_1rho relaxation time measurements (*17*), diffusion-weighted imaging, and magnetic resonance elastography (MRE) (*18*). However, these techniques often lack specificity and sensitivity, which restricts their ability to provide only structural or functional images of fibrotic livers and hampers the detection of early molecular expression changes.

The occurrence and progression of liver fibrosis are accompanied by abnormal molecular expression, metabolic changes, and eventual structural compensation. Molecular imaging offers new opportunities for precise and early diagnosis and staging of liver fibrosis (*19*, *20*). Recently, the design of sensitive and specific MRI probes targeting molecules of interest in liver fibrosis has become a research hotspot (*21*). MRI molecular probes are predominantly designed to target collagen or other components associated with the varying stages of fibrosis, showing high sensitivity and specificity in detecting fibrogenesis in various mouse models of liver fibrosis and in human fibrotic liver tissues (*22*–*25*). It is important to recognize that the progression from normal liver tissue to fibrosis is an extended process. To facilitate the early detection of liver fibrosis, there is an active effort among researchers to develop new targets for imaging. Fibrosis-related enzymes activated distance-dependent magnetic resonance tuning (MRET) nanosized probes have been reported to enable grading of liver fibrosis (*26*). The application of nanoparticles in MRET can elevate the background signal of the liver and may affect the sensitivity of the detection (*27*). Small-molecule probes with low molecular weights can be cleared from the liver if no interaction occurs, thus avoiding the issue of nonspecific aggregation. Therefore, the development of small-molecule probes with high specificity and sensitivity for imaging liver fibrosis is highly desirable.

In this study, fibroblast activation protein (FAP) was chosen as the molecular imaging target for assessing liver fibrosis, because it is specifically overexpressed on the surface of activated hepatic stellate cells (aHSCs) (*28*). The activation of HSCs is a crucial step in the development of liver fibrosis (*29*), and the level of FAP expression positively correlates with the degree of aHSCs activation and the severity of liver fibrosis (*30*). We de novo constructed a small-molecule MRI probe with a substrate moiety for FAP, named GPA-KLVFF-Gd, targeting FAP on aHSCs. GPA-KLVFF-Gd comprises three main motifs: a FAP-specific cleavage moiety, a self-assembly moiety, and an MRI imaging moiety. In fibrotic livers, the overexpressed

Department of Radiology, Tongji Hospital, Shanghai Frontiers Science Center of Nanocatalytic Medicine, The Institute for Biomedical Engineering & Nano Science, School of Medicine, Tongji University, Shanghai 200065, China.
*Corresponding author. Email: bingbozhang@tongji.edu.cn
†These authors contributed equally to this work.

FAP specifically cleaves the substrate peptide moiety to expose the self-assembly motif and lastly causes assembly of probes to nanofibers in situ. This transition not only changes the metabolic behavior of small molecule but also enhances the relaxation properties of the probe for sensitive MRI. To validate the diagnostic capabilities of GPA-KLVFF-Gd, we established two live mouse models of liver fibrosis: the bile duct ligation (BDL) model and the carbon tetrachloride (CCl_4)–induced model. Quantitative GPA-KLVFF-Gd–enhanced MRI signals demonstrated a direct correlation with the fibrosis activity in these two models, enabling noninvasive early diagnosis, precise staging, and prognosis assessment of liver fibrosis.

RESULTS

Probe construction and its response to FAP

The molecular structure of GPA-KLVFF-Gd [GTDTKTGPAKLVFF-CK(Gd-DOTA)TDTG] is depicted in Fig. 1A. In detail, it comprises a hydrophilic motif (Gly-Thr-Asp-Thr-Lys-Thr and Thr-Asp-Thr-Gly), a FAP-specific cleavage motif (Gly-Pro-Ala), a self-assembly motif (Lys-Leu-Val-Phe-Phe), and Gd-DOTA for MRI (fig. S1). The proposed imaging mechanism of GPA-KLVFF-Gd is illustrated in Fig. 1B. The FAP-specific cleavage motif can be cleaved by the overexpressed FAP on aHSCs, exposing the self-assembly motif and further inducing in situ self-assembly with a typical β-sheet structure on aHSCs in fibrotic livers. This morphologic transition from small molecules to nanofibers greatly improves the rotational correlation time (τ_R) of the probe, thus enhancing MRI signals (*31*). GPA-KLVFF-Gd–enhanced MRI allows for the visualization and quantitative assessment of FAP expression through MR signal intensity, facilitating early diagnosis and precise staging of liver fibrosis. However, in normal liver tissues, the probe is not cleaved by enzyme, thus the small GPA-KLVFF-Gd can be cleared from liver rapidly without enhanced MRI signals.

To investigate the FAP-catalyzed self-assembly behavior of GPA-KLVFF-Gd, we synthesized a non–FAP-responsive probe, namely GAA-KLVFF-Gd, by replacing the FAP-specific cleavage motif (Gly-Pro-Ala) with a nonresponsive motif (Gly-Ala-Ala) (fig. S2). A series of characterization techniques were used to assess the responsiveness of the probe toward FAP. As shown in Fig. 2 (A to C), after addition of FAP into the solution of GPA-KLVFF-Gd, a regular fibrous structure was observed. Over time, the shorter fibers further aggregated into longer fibrous assemblies. The occurrence of self-assembly was further confirmed by measuring the hydrated particle size (Fig. 2D). In contrast, the control probe GAA-KLVFF-Gd, which is not responsive to FAP, did not exhibit self-assembly behavior after incubation with FAP (fig. S3). Further, high-performance liquid chromatography (HPLC) results showed a new peak appeared at retention time of 14.0 min, while a recession occurred in 13.2 min after FAP addition. The control probe GAA-KLVFF-Gd was found to have no significant change in the HPLC curves after FAP addition (Fig. 2E).

To further explore the self-assembly behavior following FAP-specific cleavage, circular dichroism (CD) spectroscopy was used to study the structure of the assembled nanofibers. It showed a well-ordered β-sheet secondary structure with a strong positive band at 190 nm (Fig. 2F) after assembly. In addition, we used thioflavin T (ThT) to characterize the formation process of the β-sheet assembly. ThT is a benzothiazole dye that emits enhanced fluorescence upon binding to amyloid fibrils (*32*). The fluorescence patterns in Fig. 2G suggested that the FAP-treated GPA-KLVFF-Gd probe was in the growth phase of the primary process for the first 2 hours, transition to the elongation phase of the surface-catalyzed secondary process between 2 and 3 hours, and entered into a final smooth phase after 3 hours. However, the control probe did not exhibit enhanced fluorescence. These results collectively indicate that GPA-KLVFF-Gd can be cleaved by FAP and self-assembled into nanofibers with a β-sheet structure.

Moreover, the mechanism of FAP-catalyzed self-assembly of GPA-KLVFF-Gd was studied by molecular dynamics simulations on GPA-KLVFF-Gd and the postcleavage probe KLVFF-Gd [AKLVFFCK(Gd-DOTA)TDTG] in aqueous solution. For both GPA-KLVFF-Gd and KLVFF-Gd, molecular dynamics simulations were performed for 200 ns on systems composed of two peptide probes at 1 bar and 310 K. On the basis of the dynamic trajectories of the two systems and the root mean square deviation of the probes, which measures the difference between each frame of the simulation and the initial conformation, served as a criterion for determining system equilibrium (fig. S4). Selected time points with stable conformation were exported as snapshots (Fig. 3, A and C).

In GPA-KLVFF-Gd system without FAP addition, Fig. 3A showed the hydrophilic motif near the cleavage site remained close to the self-assembly motif due to hydrophobic interactions, and the modified Gd-DOTA was consistently perpendicular to the self-assembly motif. This configuration created notable steric hindrance, preventing further intermolecular assembly, while in the KLVFF-Gd system (mimic the system after the probe GPA-KLVFF-Gd is cleaved by FAP), it showed assembly occurred (Fig. 3C). The simulation data indicated parallel alignment of Gd-DOTA with the probe backbone due to the reduced steric hindrance after removal of the hydrophilic sequence, and this rearrangement eventually enhanced mutual contact of molecules in solution to form stable nanofibers. The exposed hydrophobic residues such as Phe, Val, and Leu on the self-assembly sequence exhibited extensive van der Waals interactions, promoting self-assembly. In the 200-ns snapshots of KLVFF-Gd system (Fig. 3D), two probes were observed to be tightly bound together in a typical antiparallel β-sheet configuration, with hydrogen bonds formed between AThr9-BThr9, AMK8-BThr9, and APhe6-BThr11 (fig. S5). In contrast, in GPA-KLVFF-Gd system, strong steric hindrance prevented effective self-assembly, resulting in a relatively distant and primarily parallel alignment of the self-assembly sequences between the two probes (Fig. 3B).

The radius of gyration (Rg), which measures the compactness of macromolecules, decreased more rapidly and more significantly in KLVFF-Gd system compared to GPA-KLVFF-Gd (Fig. 3E). Statistical analysis of the last 10 ns (Fig. 3F) showed an average Rg of 1.02 ± 0.05 nm for GPA-KLVFF-Gd system and 0.84 ± 0.01 nm for KLVFF-Gd, indicating a more compact assembly in the latter. Polar binding free energy, reflecting molecules hydrophilicity, showed an average polar binding free energy of 50.18 ± 17.40 kcal/mol in GPA-KLVFF-Gd system and 26.98 ± 18.55 kcal/mol in KLVFF-Gd system (Fig. 3, G and H). These data suggest the probe GPA-KLVFF-Gd after FAP-catalyzed cleavage; the resulting KLVFF-Gd has lower polar binding free energy and better binding affinity between the peptides and eventually facilitates nanofiber formation.

MRI enhancement study of GPA-KLVFF-Gd response to FAP

According to the Solomon-Bloembergen-Morgan equations of paramagnetic relaxation theory (*33*–*36*), the dominant factor of relaxivity of probes is typically the rotational correlation time (τ_R) of probes

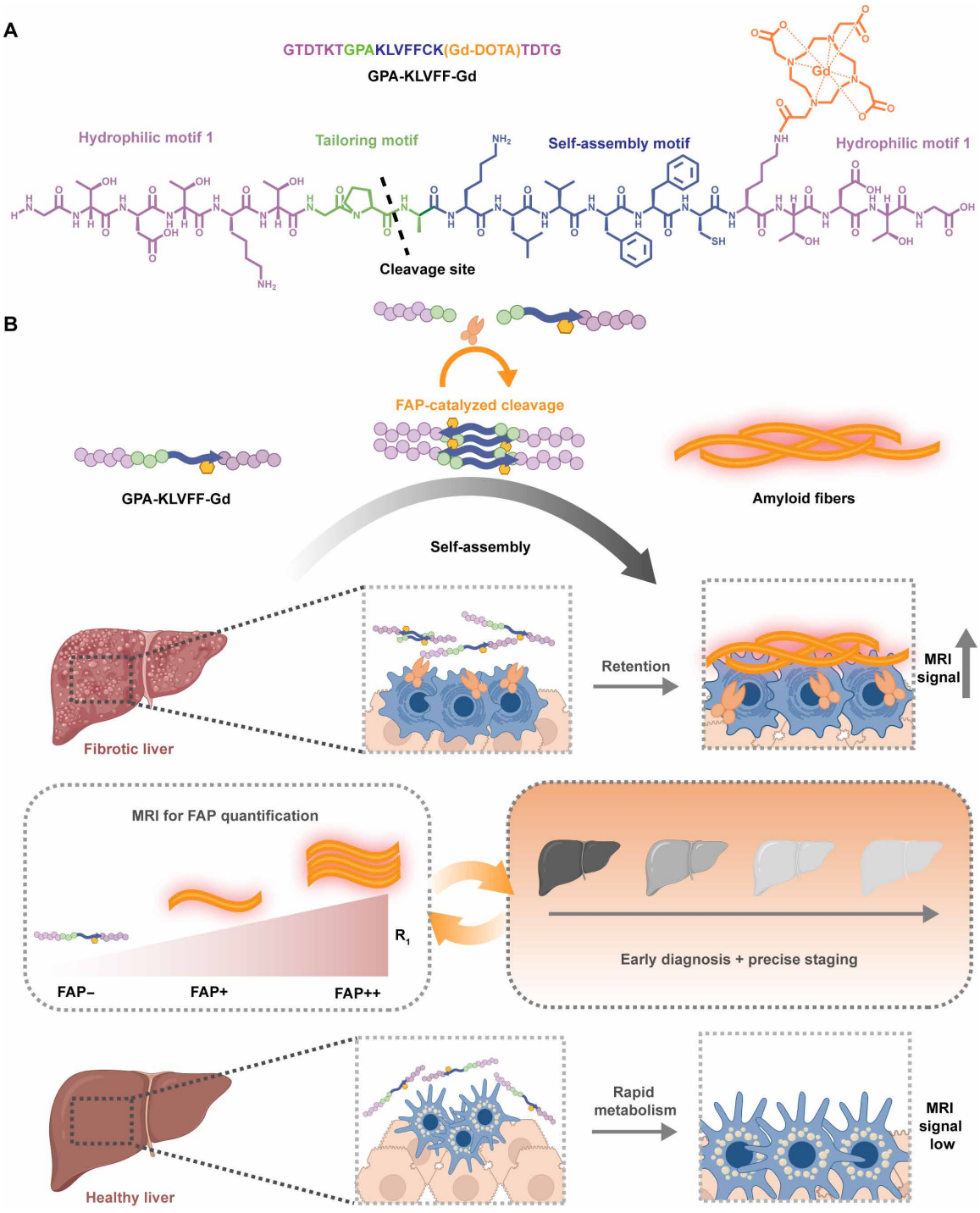

Fig. 1. Probe design. (**A**) Chemical structure of GPA-KLVFF-Gd probe. (**B**) Schematic illustration of FAP-catalyzed self-assembly of GPA-KLVFF-Gd probe to nanofibers in situ for early diagnosis and precise staging of liver fibrosis. Liver pattern and cell pattern in (B) were created with BioRender.com.

(*31*). FAP-catalyzed self-assembly can increase τ_R of GPA-KLVFF-Gd, thereby enhancing its longitudinal relaxivity and increasing the T_1-weighted MRI signal intensities (Fig. 4A). First, the in vitro MRI enhancement of GPA-KLVFF-Gd was measured under 1 T and 37°C. As shown in Fig. 4 (B and C), before FAP catalysis, the T_1-weighted MR signal intensities of the original GPA-KLVFF-Gd and GAA-KLVFF-Gd (the control probe) were found to be almost identical due to their similar structures and molecular weights, but these two probes had better signals compared to Gd-DTPA, primarily due to their larger molecular weights, which prolonged τ_R. After incubation with FAP, only GPA-KLVFF-Gd showed enhanced T_1 MR signals, while the signal intensities of Gd-DTPA and GAA-KLVFF-Gd

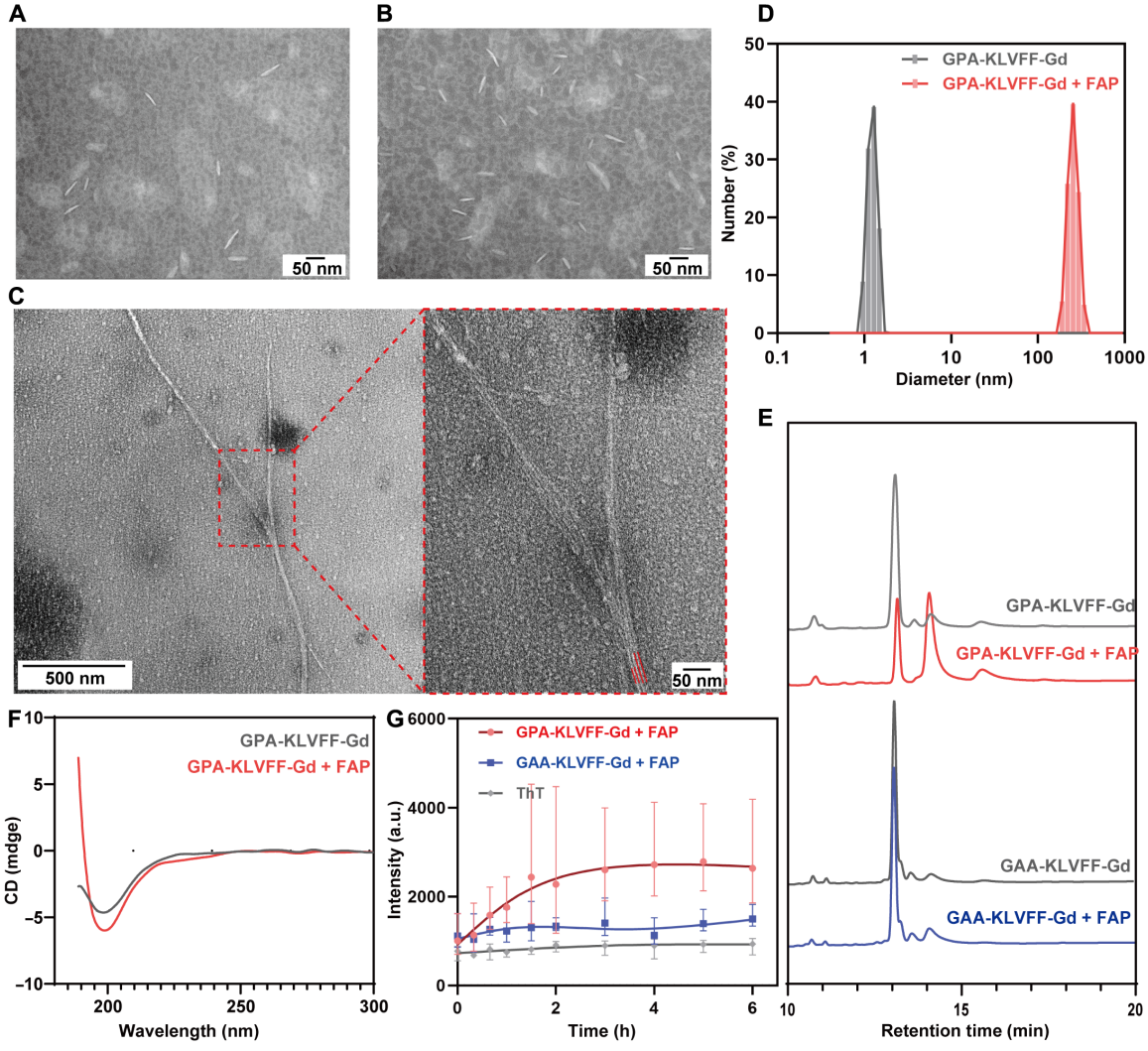

Fig. 2. FAP-catalyzed self-assembly behavior and assembled structure conformations of GPA-KLVFF-Gd. TEM images of GPA-KLVFF-Gd after 1 (**A**) and 3 hours (**B**) of incubation with FAP, and after 6 hours (**C**) of incubation with FAP. (**D**) Hydrodynamic size of GPA-KLVFF-Gd and GPA-KLVFF-Gd incubated with FAP. (**E**) HPLC curves of GPA-KLVFF-Gd and GAA-KLVFF-Gd before and after 12 hours of incubation with FAP. (**F**) CD spectra of GPA-KLVFF-Gd before (black line) and after (red line) incubation with FAP. (**G**) Dynamic FAP tailoring and assembly of GPA-KLVFF-Gd compared to GAA-KLVFF-Gd and ThT in buffer.

remained unchanged. Subsequently, we characterized the kinetic changes in enzymatic self-assembly–enhanced MR signals by monitoring longitudinal relaxation times of the probes. Upon adding FAP, the longitudinal relaxation times of GPA-KLVFF-Gd rapidly decreased within the first 4 hours, reaching a plateau after 6 hours, while the longitudinal relaxation times of GAA-KLVFF-Gd remained unchanged (Fig. 4D). Without FAP incubation, both GPA-KLVFF-Gd (0.19 mM) and GAA-KLVFF-Gd (0.19 mM) exhibited good stability within 24 hours at 37°C, which have been confirmed by T_1, T_2, and size monitoring (fig. S6). These results suggest that FAP-catalyzed self-assembly of GPA-KLVFF-Gd shortens its longitudinal relaxation time, thereby enhancing the T_1 MR signals. In particular, with increasing FAP concentration, GPA-KLVFF-Gd displayed a typical T_1-weighted brightening pattern (Fig. 4, E and F). This positive correlation between the FAP concentration and the MRI intensity favors staging liver fibrosis.

The selectivity and stability of GPA-KLVFF-Gd were investigated by incubating the probe in solutions containing alkaline phosphatase (ALP), glutathione (reduced form) (GSH), H_2O_2, or serum albumin. ALP, GSH, and H_2O_2 are also biomarkers of liver-related diseases; therefore, they were chosen to verify the selectivity of the probe for FAP. Serum albumin was selected to verify the stability of the probe in blood because it is the most abundant protein in the circulatory system. Untreated probe and the probe treated with FAP served as negative or positive controls, respectively. After incubation at 37°C for 6 hours, a marked increase in T_1-weighted brightening was observed in the FAP-treated group, while no significant enhancement was seen in the groups with interfering substances (Fig. 4, G and H). These results indicate that GPA-KLVFF-Gd has high selectivity toward FAP and robust resistance to interferences from common biomolecules in body.

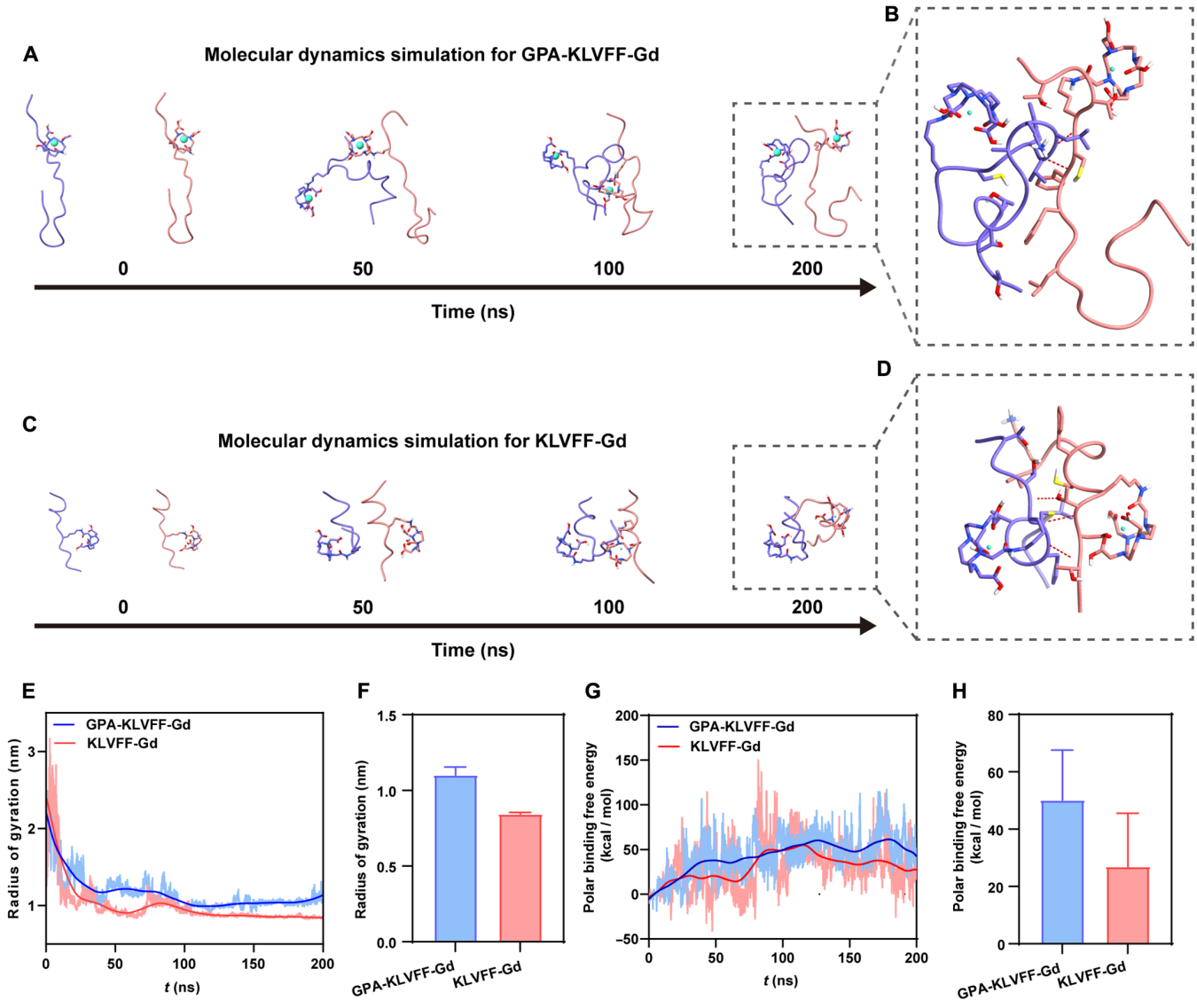

Fig. 3. MD simulation of GPA-KLVFF-Gd and KLVFF-Gd. Snapshots of the GPA-KLVFF-Gd system (**A**) and KLVFF-Gd system (**C**) at 0, 50, 100, and 200 ns. Details of peptide interactions in the GPA-KLVFF-Gd system (**B**) and KLVFF-Gd system (**D**) at 200 ns. Time-dependent Rg curves of GPA-KLVFF-Gd system (blue line) and KLVFF-Gd system (red line) (**E**) and corresponding average of last 10 ns (**F**). Time-dependent polar binding free energy curves of GPA-KLVFF-Gd system (blue line) and KLVFF-Gd system (red line) (**G**) and the corresponding average of last 10 ns (**H**).

Last, we quantitated the relaxivity of the designed probe before and after FAP catalysis. After incubation with FAP (20 nM, 6 hours), the longitudinal relaxivity (r_1, 1.41 T, 37°C) of GPA-KLVFF-Gd increased from 9.09 to 17.14 $mM^{-1}{\cdot}s^{-1}$ (Fig. 4I), and the transverse relaxivity (r_2, 1.41 T, 37°C) increased from 10.68 to 25.51 $mM^{-1}{\cdot}s^{-1}$ (Fig. 4J). In contrast, both r_1 and r_2 of the uncleavable GAA-KLVFF-Gd remained almost unchanged. These results demonstrate that GPA-KLVFF-Gd exhibits high selectivity toward FAP and superior activatable MRI capability, which is crucial for cellular and in vivo imaging of FAP.

In vitro FAP-catalyzed MRI enhancement in aHSCs

Before assessing the responsiveness of GPA-KLVFF-Gd to FAP using the rat HSC-T6 HSC line as a model, we first validated the low cytotoxicity of GPA-KLVFF-Gd (fig. S7). Untreated HSC-T6 cells, serving as the control group, consist of quiescent HSCs (qHSCs) that barely express FAP. The fibroblast growth factor transforming growth factor–β-1 (TGFβ-1) was used to induce these cells into aHSCs that overexpress FAP (*37*). Initially, HSC-T6 cells were coincubated with culture medium containing varying concentrations of TGFβ-1 for 24 hours to induce activation into aHSCs with different levels of FAP expression. Subsequently, the probe was added to the culture medium and coincubated with the cells for 12 hours, followed by MRI and scanning electron microscopy (SEM) to verify the probe's ability to enhance MRI and self-assemble in response to FAP at the cellular level (Fig. 5A). FAP expression was confirmed by immunofluorescence (Fig. 5B). To be specific, in untreated cells, FAP-positive cells were virtually unobservable. However, in cells treated with TGFβ-1, FAP-positive aHSCs was distinctly observed, with the proportion of FAP-positive aHSCs positively correlating with the concentration of TGFβ-1 (Fig. 5C).

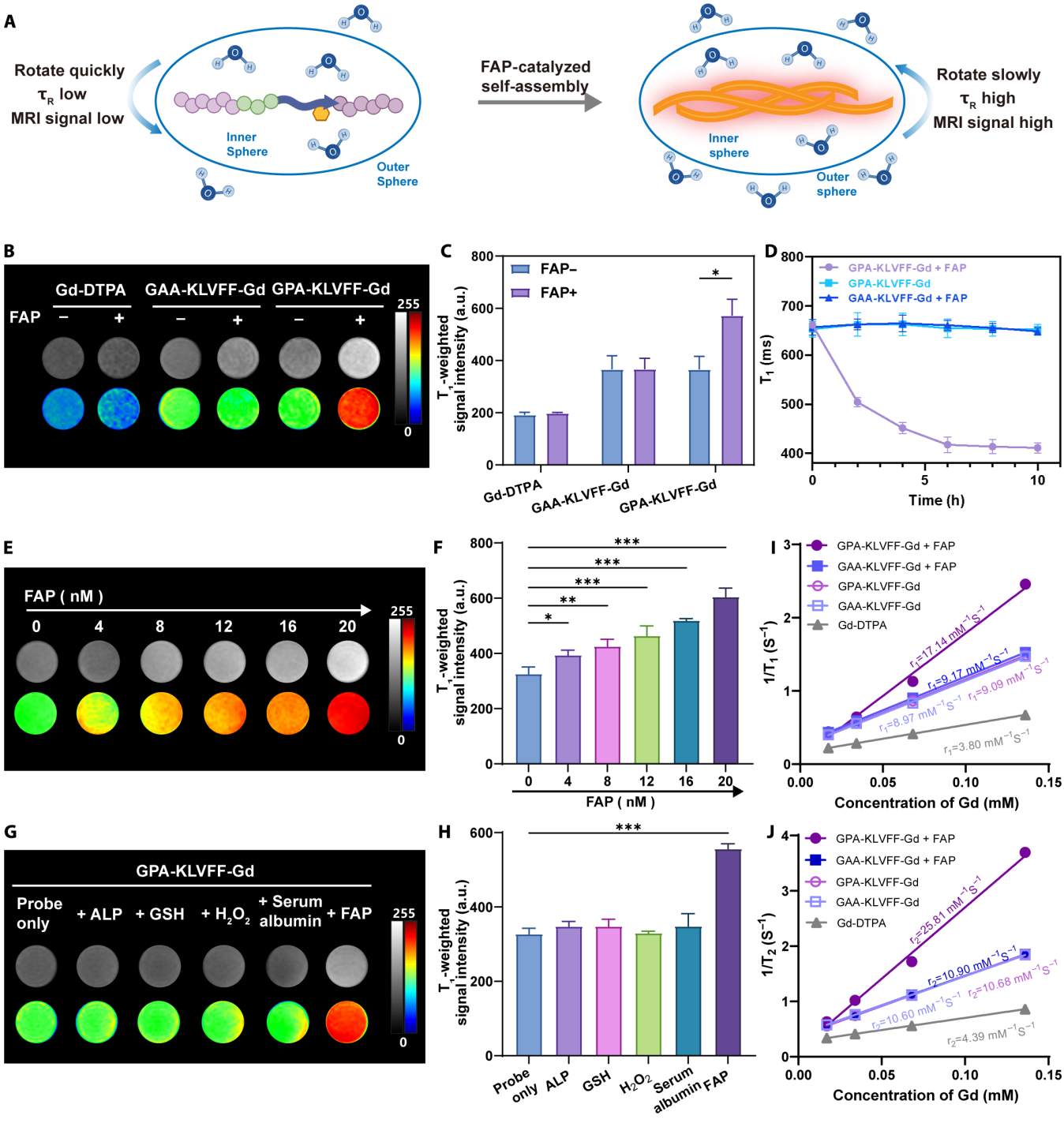

Fig. 4. FAP-catalyzed T_1-weighted MRI enhancement study. (**A**) Schematic illustration of FAP-catalyzed self-assembly enhancing MRI signal. T_1-weighted MRI images (**B**) and T_1-weighted MRI signal intensity (**C**) of Gd-DTPA, GAA-KLVFF-Gd, and GPA-KLVFF-Gd before and after incubation with FAP (20 nM, 6 hours). (**D**) Longitudinal times of GPA-KLVFF-Gd and GAA-KLVFF-Gd after the addition of FAP. FAP concentration–dependent T_1-weighted MRI images (**E**) and T_1-weighted MRI signal intensity (**F**) of GPA-KLVFF-Gd. T_1-weighted MRI images (**G**) and T_1-weighted MRI intensity (**H**) after incubation with different analytes for 6 hours. Longitudinal (**I**) and transverse relaxation (**J**) rates of Gd-DTPA, GPA-KLVFF-Gd, and GAA-KLVFF-Gd before and after incubation with FAP (20 nM, 6 hours). The relaxivity measurements were conducted at 37°C and 1.41 T (Minispec mq 60, Bruker, Germany). Data shown as means ± SD; *$P < 0.05$, **$P < 0.01$, and ***$P < 0.001$; ns, not significant.

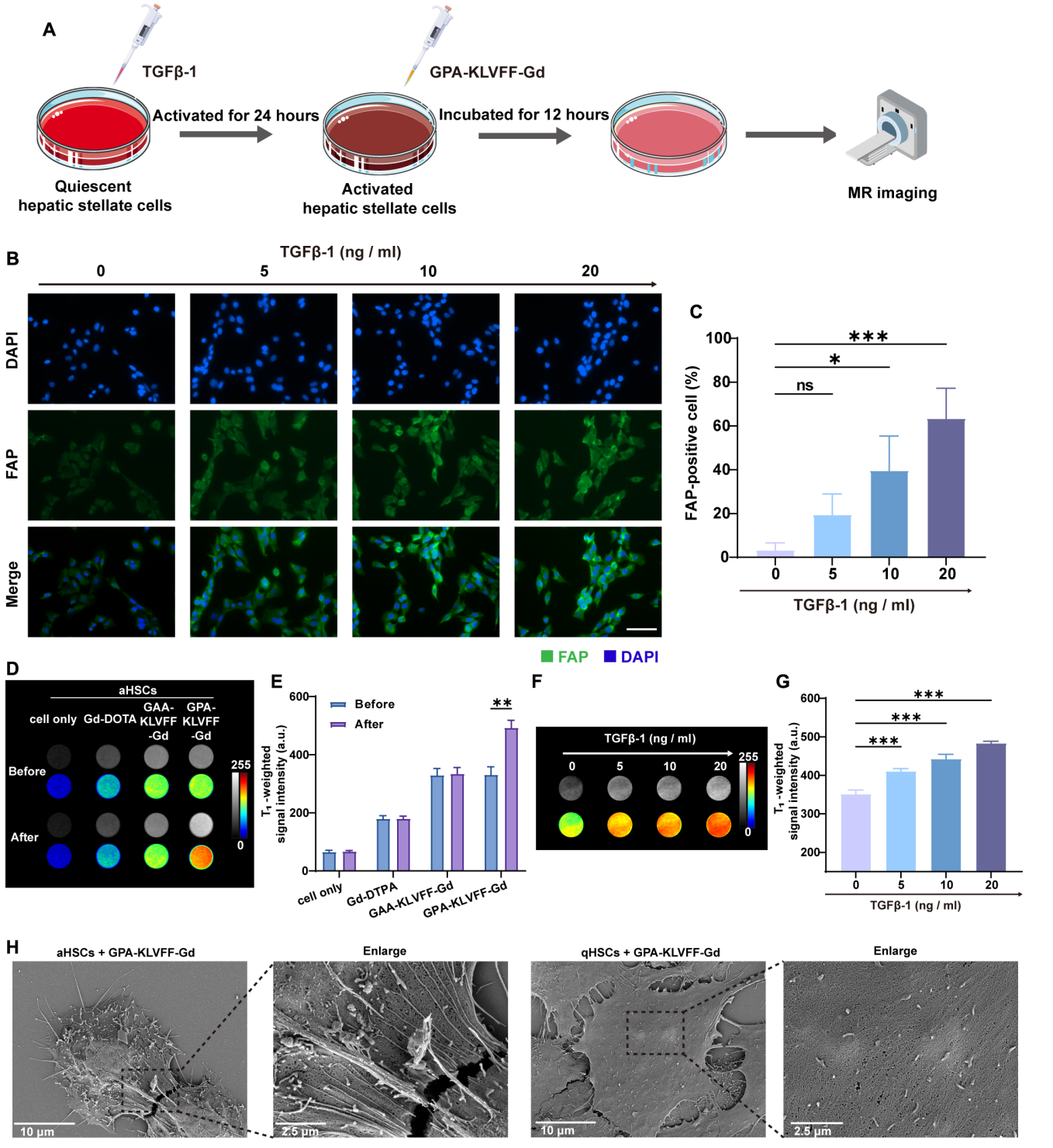

Fig. 5. FAP-catalyzed MR imaging enhancement in cells. (**A**) Schematic illustration of procedure for MR imaging and bio-SEM analysis of the in situ self-assembly on activated HSCs. (**B**) Representative immunofluorescence images showing the activation degree of HSC-T6 cells by TGFβ-1 (0, 5, 10, and 20 ng/ml). Green indicates FAP expression. Scale bar, 50 μm. (**C**) Analysis of the proportion of FAP-positive cells in HSC-T6 cells treated with different concentrations of TGFβ-1 (0, 5, 10, and 20 ng/ml). T_1-weighted MRI images (**D**) and corresponding signal intensity histograms (**E**) before and after coincubation (0.19 mM, 12 hours) of different probes (Gd-DOTA, GAA-KLVFF-Gd, and GPA-KLVFF-Gd) with activated HSCs. T_1-weighted MRI images (**F**) and corresponding signal intensity histograms (**G**) before and after GPA-KLVFF-Gd coincubation (0.19 mM, 12 hours) with HSCs at different activation degrees. (**H**) SEM images of activated and quiescent HSC-T6 cells treated with 0.19 mM GPA-KLVFF-Gd at 37°C for 12 hours. Data shown as means ± SD; $^*P < 0.05$, $^{**}P < 0.01$, and $^{***}P < 0.001$; ns, not significant.

Figure 5 (D and E) showed that only GPA-KLVFF-Gd probe-incubated cells displays increased T_1-weighted brightening and signal intensity, demonstrating its good specific responsiveness to FAP overexpressed on aHSCs. We further validated the sensitivity of GPA-KLVFF-Gd at the cellular level by coincubation with HSC-T6 cells, which were pre-activated by different concentrations of TGFβ-1 (0, 5, 10, and 20 ng/ml) for 12 hours. It showed that the MRI signal intensity was positively related to the TGFβ-1 concentration for HSC-T6 activation (Fig. 5, F and G). In situ self-assembly of nanofiber network was observed on the membrane of aHSCs after incubating with GPA-KLVFF-Gd by using SEM (Fig. 5H). However, no nanofiber structure was detected on the membrane surface of untreated HSC-T6 cells (qHSCs). These results intuitively demonstrates that GPA-KLVFF-Gd can undergo in situ self-assembly on cells post-catalysis by FAP, transforming small molecules to nanofibers, prolonging τ_R and thereby enhancing T_1-weighted MRI signals.

Precise staging of BDL-induced liver fibrosis in vivo

Cholestasis is a major cause of liver fibrosis and cirrhosis in acute and chronic liver diseases (*38*). BDL is the most commonly used method to replicate biliary obstructive cholestasis-induced liver fibrosis models. Before testing on BDL model, we tested the liver metabolism of GPA-KLVFF-Gd in healthy mice and it showed that GPA-KLVFF-Gd can be rapidly cleared from liver and excluded into bladder like Gd-DTPA (fig. S8). This rapid clearance can notably reduce nonspecific signal enhancement caused by liver retention, thus avoiding false-positive signals.

Mice underwent T_1-weighted MRI at 1 and 2 weeks post-BDL surgery (Fig. 6A). Liver fibrosis stages were graded using immunohistochemistry and the Ishak semi-quantitative scoring system (*39*, *40*). Figure 6B showed T_1-weighted MR images of healthy mice and those with different stages of liver fibrosis after intravenous injection of GPA-KLVFF-Gd, GAA-KLVFF-Gd, and the clinical Gd-DTPA. Quantitative analysis was conducted using the signal intensity measured by the Niumag NMR Image Processing Software after being self-normalized, with ΔSNR% serving as the quantified physical quantity. The quantitative data in Fig. 6C showed that GPA-KLVFF-Gd–enhanced MR images exhibited varying increases of ΔSNR% in the liver post-BDL surgery model. Compared to the ΔSNR% = 6.06 ± 2.82% in healthy mice, liver ΔSNR% significantly increased to 49.87 ± 9.95% ($P < 0.001$) in mice with early-stage liver fibrosis (Ishak stage 2 of 6) at 1-week postsurgery. In late-stage liver fibrosis (Ishak stage 5 of 6) at 2-week postsurgery, the liver ΔSNR% was found to be significantly increased to 118.8 ± 19.39% ($P < 0.001$). No remarkable changes in ΔSNR% were observed in late-stage liver fibrosis mice (2-week post-BDL surgery) injected with two control probes, namely, GAA-KLVFF-Gd and Gd-DTPA. The in vivo distribution of GPA-KLVFF-Gd and GAA-KLVFF-Gd in late-stage liver fibrosis mice indicated that the cleavable GPA-KLVFF-Gd can be retained more in fibrotic livers (fig. S9). In addition, time-course curve of ΔSNR% obtained by GPA-KLVFF-Gd indicated that as liver fibrosis worsens, a higher ΔSNR% and a longer retention time in livers were observed (figs. S10 and S11).

Next, we conducted histopathological analysis to demonstrate the self-assembly of GPA-KLFF-Gd in fibrotic liver. Congo red is a histological standard for amyloid fibers in clinical analysis, which can bind to amyloid fibrils (β-sheet structure nanofibers) to form red compounds (*41*, *42*). Few red staining was seen in GPA-KLVFF-Gd–injected healthy mice livers, while GPA-KLVFF-Gd–injected fibrotic liver mice showed red deposits around the sinusoids, confirming that the probe indeed self-assembly in fibrotic liver tissues (fig. S12). Moreover, we used SEM to visualize the in situ self-assembly of GPA-KLVFF-Gd and the morphology of treated livers (fig. S13). SEM images showed no significant changes on healthy mice liver cell surfaces before and after GPA-KLVFF-Gd injection, while complex nanofiber network scaffolds orchestrated by GPA-KLVFF-Gd were observed on cell surfaces in fibrotic liver mice postinjection. These results indicated that the FAP-catalyzed self-assembly of GPA-KLVFF-Gd can lead to an effective accumulation and retention in fibrotic liver, thereby enhancing MRI signal of fibrotic liver.

Histological analysis (Fig. 6D) using the Ishak scoring system confirmed that mice exhibited early stage of liver fibrosis (Ishak score = 2) at 1-week post-BDL surgery and late stage of liver fibrosis (Ishak score = 5) at 2-week post-BDL surgery. Immunohistochemical staining further assessed the activation degree of HSCs [α–smooth muscle actin (α-SMA)] and the expression of FAP in liver tissues (Fig. 6E). Both α-SMA (red) and FAP (green) expression levels were higher in BDL-induced mice than in healthy mice and this trend increased with prolonged induction time. Quantitative analysis revealed that after 1 and 2 weeks of BDL surgery, Sirius red–positive tissue increased from 0.40 ± 0.25% in healthy mice to 7.69 ± 1.69% and 12.74 ± 1.32%, respectively (Fig. 6F). Similarly, the α-SMA–positive area increased from 0.70 ± 0.38% to 5.01 ± 1.44% and 12.23 ± 3.27% (Fig. 6G). The FAP-positive area also showed a marked increase, rising from 0.79 ± 0.69% to 5.78 ± 0.44% and 13.9 ± 1.67% after 1 and 2 weeks of BDL surgery, respectively (Fig. 6H). On the basis of these measurements, a linear regression model was set between liver ΔSNR% and various fibrosis-related immunohistochemical biomarkers and FAP expression. The analysis revealed a strong correlation between ΔSNR% and the proportion of Sirius red–positive tissue ($R = 0.79$; Fig. 6I), α-SMA–positive tissue ($R = 0.92$; Fig. 6J), and FAP-positive tissue ($R = 0.89$; Fig. 6K).

For comparison, ultrasound imaging was used to assess the liver injury of mice at various stages of fibrosis post-BDL surgery (fig. S14). Only a slight increase in echogenic signals was observed in the livers of late-stage fibrosis, apparently at least a week after our probe in this study, indicating that ultrasound imaging has obvious limitations in the early diagnosis and staging of liver fibrosis. This low sensitivity imaging is mainly subject to the principle of structural imaging. Structural changes usually do not occur until the advanced stages of the disease. By contrast, the use of molecular imaging can detect molecular expression abnormalities at an earlier stage of disease.

Precise staging and evaluation of treatment responses in the CCl_4-induced liver fibrosis in vivo

We further examined the sensitivity of GPA-KLVFF-Gd for early imaging of liver fibrosis and its responsiveness to therapeutic intervention in carbon tetrachloride (CCl_4)–induced mouse model. CCl_4 administration can cause liver damage with increased weight, fat, urea, and enzyme levels, progressing to fibrosis and cirrhosis, but can be reversed by treatment cessation or drug therapy (*43*). Mice were administered CCl_4 through intraperitoneal injections twice a week for 3, 5, or 10 weeks. Two additional groups received CCl_4 for 10 weeks and then discontinued CCl_4 and treated with resveratrol (Res), a drug that inhibits HSCs activation (*44*), for 1 or 3 weeks (Fig. 7A). Figure 7B displayed T_1-weighted subtraction images of 15 min after GPA-KLVFF-Gd injection in both control and CCl_4 groups, revealing a progressive increase in ΔSNR% with extended

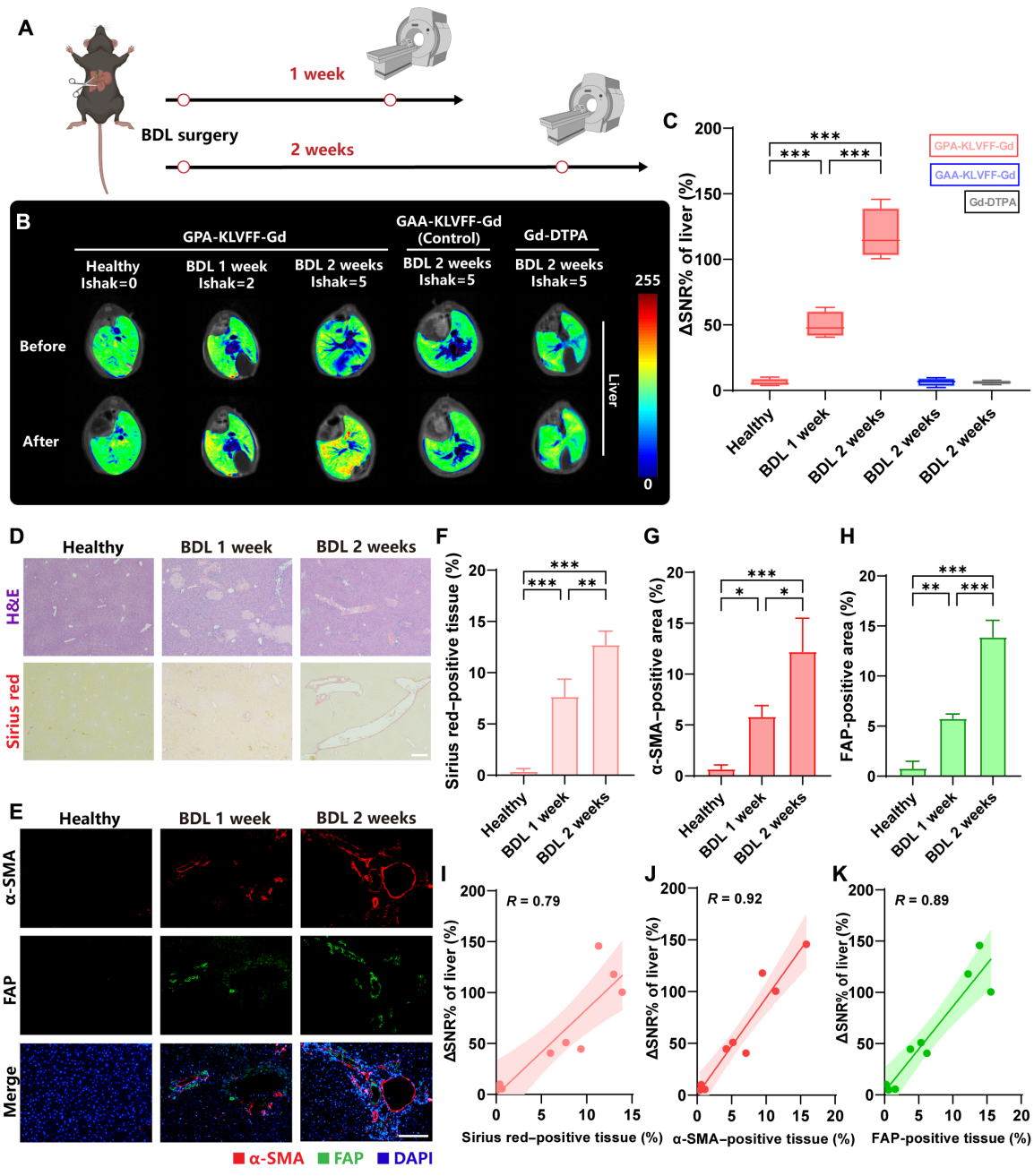

Fig. 6. GPA-KLVFF-Gd for precise staging of BDL-induced liver fibrosis. (**A**) At 1 and 2 weeks after BDL surgery, mice were imaged after intravenous injection of GPA-KLVFF-Gd, GAA-KLVFF-Gd, and Gd-DTPA, followed by euthanasia and ex vivo characterization of the liver. (**B**) T_1-weighted MR images of livers in healthy mice (Ishak stage 0 of 6), early-stage (Ishak stage 2 of 6), and late-stage liver fibrosis (Ishak stage 5 of 6) before and 15-min after injection of GPA-KLVFF-Gd and late-stage liver fibrosis (Ishak stage 5 of 6) before and 15-min after injection of GAA-KLVFF-Gd and Gd-DTPA. (**C**) Quantitative measurement ΔSNR% of the liver T_1-weighted MR images (all data are shown as means ± SD; $^*P < 0.05$, $^{**}P < 0.01$, and $^{***}P < 0.001$; ns, not significant). (**D**) Representative H&E and Sirius red staining of livers from BDL-induced mice. Scale bar, 200 μm. (**E**) Representative immunohistochemical staining for FAP in liver tissues from normal and BDL mice. Scale bar, 50 μm. (**F**) The percentage of Sirius red–positive tissue measured from Sirius red staining livers (data shown as means ± SD; $^*P < 0.05$, $^{**}P < 0.01$, and $^{***}P < 0.001$; ns, not significant). (**G**) The percentage of α-SMA–positive tissue measured from immunohistochemical staining for aHSCs in liver tissues (data shown as means ± SD; $^*P < 0.05$, $^{**}P < 0.01$, and $^{***}P < 0.001$; ns, not significant). (**H**) The percentage of FAP-positive tissue measured from immunohistochemical staining for FAP in liver tissues (data shown as means ± SD; $^*P < 0.05$, $^{**}P < 0.01$, and $^{***}P < 0.001$; ns, not significant). Correlation analysis between ΔSNR% at 15 min and Sirius red–positive tissue (**I**) ($R = 0.79$, $P < 0.001$), α-SMA–positive tissue (**J**) ($R = 0.92$, $P < 0.001$), and FAP-positive tissue (**K**) ($R = 0.89$, $P < 0.001$).

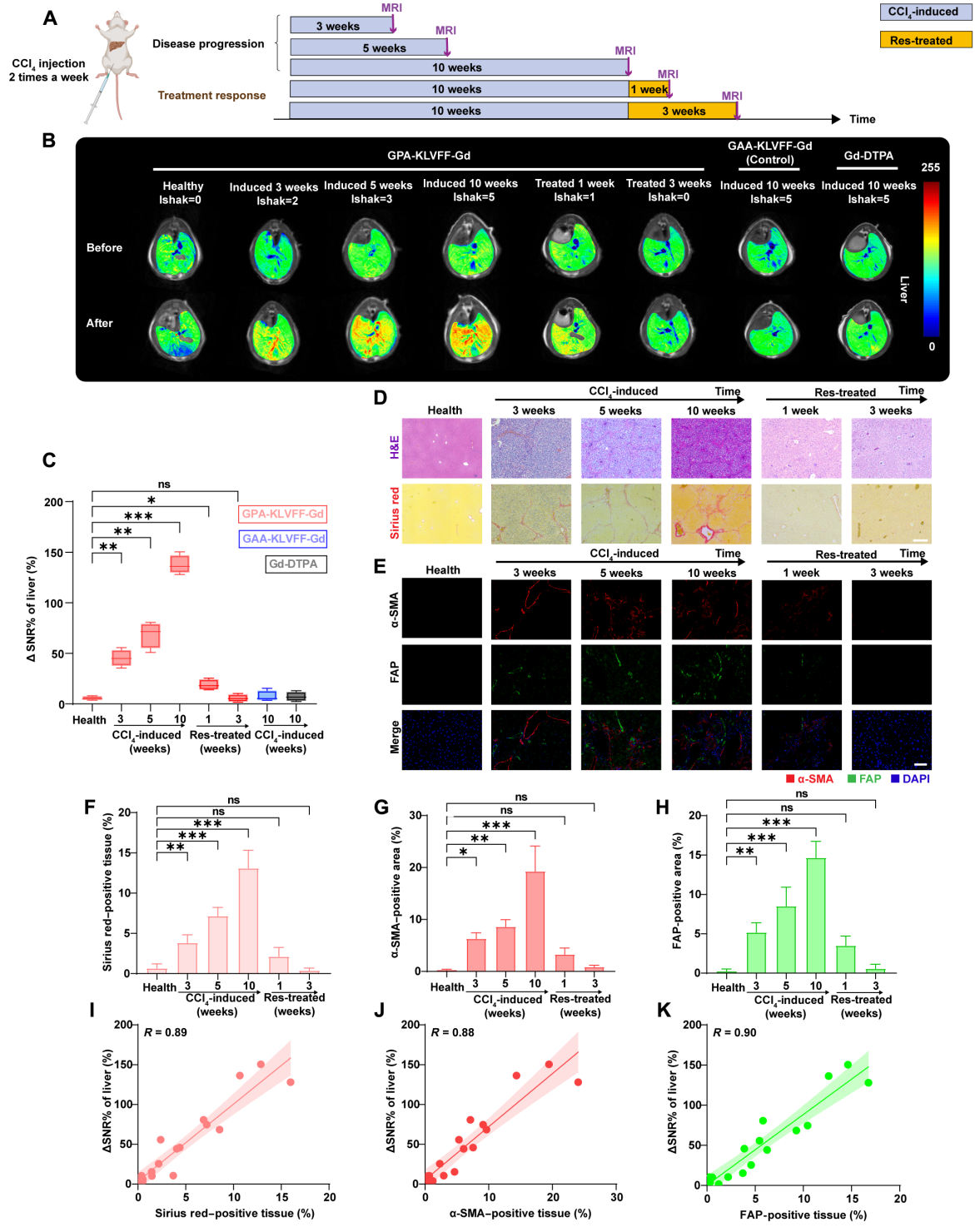

Fig. 7. GPA-KLVFF-Gd for precise staging and evaluation of treatment responses in the CCl_4-induced liver fibrosis. (**A**) The diagram outlines experimental design, animal group classification, and in vivo MRI. Mice received intraperitoneal CCl_4 injections twice a week for 3, 5, and 10 weeks to study the progression of toxin-mediated liver fibrosis. After 10 weeks, CCl_4 administration was discontinued and Res treatment was given for 1 or 3 weeks to study treatment response. At each time point, mice underwent GPA-KLVFF-Gd–, GAA-KLVFF-Gd–, or Gd-DTPA–enhanced MRI, followed by euthanasia and ex vivo liver characterization. (**B**) Subtraction T_1-weighted images (difference between 15 min postinjection and preinjection in healthy and CCl_4-induced groups. (**C**) Quantitative analysis of liver to noise ΔSNR% at 15 min in each group (data shown as means ± SD; $^*P < 0.05$, $^{**}P < 0.01$, and $^{***}P < 0.001$; ns, not significant). (**D**) Representative H&E and Sirius red staining of livers from healthy and CCl_4-induced mice. Scale bar, 200 μm. (**E**) Immunohistochemical staining for the HSCs activation degree (α-SMA, red) and the of FAP expression (green) from healthy mice and CCl_4-induced mice. Scale bar, 100 μm. The percentage of Sirius red–positive tissue (**F**), α-SMA–positive tissue (**G**), and FAP-positive tissue (**H**) in liver samples. Correlation analysis between ΔSNR% at 15 min and Sirius red–positive tissue (**I**) ($R = 0.89$, $P < 0.001$), α-SMA–positive tissue (**J**) ($R = 0.88$, $P < 0.001$), and FAP-positive tissue (**K**) ($R = 0.90$, $P < 0.001$).

CCl_4 administration, with significantly higher ΔSNR% values observed in the livers of CCl_4-induced mice as early as 3 weeks (ΔSNR% = 45.30 ± 8.23%, $P < 0.01$) compared to healthy mice (ΔSNR% = 5.56 ± 1.88%). The ΔSNR% of the MR images of fibrotic mouse livers for Ishak = 3 and Ishak = 5 is 68.68 ± 12.86% and 137.60 ± 9.38%, respectively. However, even in late-stage liver fibrosis mice (Ishak score = 5, treated with CCl_4 for 10 weeks), it did not show a significant increase in ΔSNR% 15-min postinjection of GAA-KLVFF-Gd or Gd-DTPA (Fig. 7C). Moreover, in the treatment model, we found that GPA-KLVFF-Gd was sensitive to the treatment. Discontinuing CCl_4 and administering Res for 1 week significantly reduced ΔSNR% (from 137.60 ± 9.38% to 18.81 ± 5.27%), which further decreased after 3 weeks of Res treatment (to 5.59 ± 3.75%).

Molecular pathological analysis confirmed the validity of our model. Histological analyses (Fig. 7D) showed that mild fibrotic changes, indicated by red areas in Sirius red staining, were present after 3 weeks of CCl_4 administration and increased with prolonged administration (Fig. 7F). Immunohistochemical staining assessed the activation degree of HSCs (α-SMA, red) and the expression of FAP (green) in both healthy and CCl_4-induced mice (Fig. 7E), showing an increase in both biomarkers with the duration of CCl_4 administration (Fig. 7, G and H). After discontinuing CCl_4 administration and treating with Res, there was a significant reduction in fibrotic tissue, HSCs activation, and FAP expression levels after 1 week of treatment. After 3 weeks of Res treatment, all parameters approached normal levels. On the basis of this, a linear regression model was set between the liver ΔSNR% and various fibrosis-related immunohistochemical biomarkers and FAP expression.

It showed that ΔSNR% acquired by GPA-KLVFF-Gd closely tracked measures of fibrogenesis, such as Sirius red–positive tissue ($R = 0.89$; Fig. 7I), α-SMA–positive tissue ($R = 0.88$; Fig. 7J), and FAP expression ($R = 0.90$; Fig. 7K). This good correlation indicates the developed GPA-KLVFF-Gd can effectively monitor liver fibrosis progression and treatment response.

Biocompatibility study of GPA-KLVFF-Gd in vivo

To evaluate the biocompatibility of GPA-KLVFF-Gd in vivo, blood was collected for biochemistry and hematology assays, and major organs (hearts, liver, spleen, lung, and kidneys) were isolated for histology analysis. One day after injection, organ function biomarker parameters (fig. S15, A and B) and hematological biomarkers (fig. S15C) showed no statistically significant differences compared to the untreated groups and were within normal reference ranges, indicating negligible toxicity of GPA-KLVFF-Gd. Hematoxylin and eosin (H&E) staining results revealed no obvious lesions in the tissues of major organs compared with the untreated groups, further indicating low toxicity of GPA-KLVFF-Gd in vivo (fig. S15D).

DISCUSSION

Liver fibrosis is a crucial stage in the progression of most chronic liver diseases. If untreated in time, it can progress to cirrhosis, liver cancer, liver failure, and even death. Currently, few noninvasive and sensitive technology is available that can diagnose early liver fibrosis and monitor its progression and response to treatment. Molecular MRI is gaining increasing attention as a diagnostic tool due to its capability in detecting molecular abnormal expression in early stage of diseases in a noninvasive manner. Despite some progress in molecular MRI for detecting liver fibrosis, challenges remain. One of the most key issues is the selection of diagnostic targets. Current studies often focus on the inflammatory stage before fibrosis onset or the type II collagen formation stage within fibrosis (*45*–*47*). These targets either lack specificity or are late in the diagnostic window. Another requirement is developing sensitive imaging probes. Nanoprobes have been widely used to improve MRI performance, but the high liver uptake leads to a notable increase in background signal (*48*–*51*), which is easy to cause false positive in the diagnosis of fibrosis. Therefore, the development of small-molecule probes is imperative.

In this study, the above two critical issues were addressed by de novo construction of FAP-catalyzed probe. We selected FAP as the imaging target as it expresses on aHSCs in the very early liver fibrosis progression. We constructed a FAP-targeting in situ self-assembly probe GPA-KLVFF-Gd, in which the peptide GPA is very specific to FAP in liver fibrosis tissues. In other words, the probe cannot be catalyzed into nanofibers in normal liver tissues, avoiding liver accumulation and preventing false positives in diagnosis. Using a battery of experimental techniques, we have clarified the imaging mechanism. In fibrotic livers, the probe undergoes catalysis by the overexpressed FAP on aHSCs, resulting in the self-assembly into nanofibers. This specific assembly increases the rotational correlation time of the probe, which in turn, amplifies the MR signals specifically in the fibrotic areas. This enhancement is not replicated in the setting of a normal liver. Moreover, the GPA-KLVFF-Gd–enhanced MRI signal was found positively related to the FAP expression on aHSCs.

Thanks to the specificity and efficiency of enzymatic reactions, GPA-KLVFF-Gd specifically detected early-stage liver fibrosis in BDL- and CCl_4-induced mouse models. Our results show that this strategy enables earlier liver fibrosis imaging than ultrasound imaging. Such improvement is mainly due to the selection of imaging target (FAP) and the unique structure of the probe we designed, which can amplify the imaging signals for higher ΔSNR%. Moreover, by setting a linear correlation between T_1 signals and liver fibrosis degrees in these models, the probe can monitor liver fibrotic disease activity during progression and even in response to drug treatment, enabling precise diagnosis and staging of liver fibrosis, real-time evaluating drug efficacy, predicting disease outcomes, and adjusting treatment strategies. Nevertheless, it is imperative to acknowledge the inherent challenges associated with the precise quantification of MRI signals. Consequently, the fibrosis staging framework introduced in this study serves as a preliminary benchmark, warranting further investigation and refinement to enhance its accuracy and applicability.

In conclusion, we have provided a noninvasive molecular MRI probe for diagnosis of incipient liver fibrosis and staging. By selecting the molecular signature of early fibrosis, FAP, as a target for imaging, and leveraging enzymatic reaction strategy, we have de novo synthesized a small-molecular probe with unique structure. Upon FAP-catalyzed cleavage, this probe undergoes transformation into nanofibers, which modulates its rotational correlation time to synchronize with the proton Larmor frequency, substantially enhancing the MRI signal subject to the target areas in vivo. This method achieves ultrasensitive and specific imaging of FAP in two liver fibrosis mouse models, exhibiting the ability to detect the onset of fibrosis at earlier stages compared to conventional ultrasound imaging technique. The proposed imaging protocol offers a beneficial reference for the early diagnosis, staging, and visualization of therapeutic efficacy in liver fibrosis and analogous conditions.

MATERIALS AND METHODS

Materials

All Fmoc-protected amino acids, *O*-(benzotriazol-1-yl)-*N*,*N*,*N*′,*N*′-tetramethyluronium hexafluorophosphate (HBTU) trifluoroacetic acid (TFA), 1,2ethanedithiol, dimethyl formamide (DMF), dichloride methane (DCM), piperidine, *N*-methylmorpholine, diethyl ether, dimethyl sulfoxide, $GdCl_3{\cdot}6H_2O$, sodium hydroxide (NaOH), carbon tetrachloride (CCl_4), and olive oil are bought from Aladdin Company. FAP (cat. no. C14G) and TGFβ-1 (cat. no. CK33) were purchased from Novoprotein (Shanghai, China). FAP-α rabbit pAb was purchased from Affinity Biosciences. Carbon tetrachloride (CCl_4) was purchased from Aladdin Company. ThT was acquired from Sigma-Aldrich. Cell counting kit–8, tris-HCl, and phosphate-buffered saline were purchased from Beyotime Biotechnology. HSC-T6 cells were purchased from Wuhan Pricella Biotechnology Co. Ltd.

Synthesis of materials

The synthesis primarily uses an automated peptide synthesizer, using the solid-phase synthesis method to construct peptide modules. Fmoc(9-fluorenylmethoxycarbonyl)-Wang resin is used as the solid support, and different amino acids are sequentially added from the C terminus to the N terminus according to the peptide sequence. During the process, a DMF solution containing 20% piperidine is used for Fmoc deprotection, and HBTU, HoBt, and DIEA are used as coupling agents for the condensation of amino and carboxyl groups. Throughout the synthesis, the resin is repeatedly washed with DMF and DCM to remove residual reactants, preventing the formation of impurities and side reactions. The product is precipitated using diethyl ether in an ice bath, centrifuged to remove the solvent, and the product is repeatedly washed with diethyl ether. The product is then dried overnight in a vacuum desiccator. The crude peptide obtained is analyzed and purified using reversed-phase HPLC.

Material characterizations

Transmission electron microscope (TEM) images of the nanofibers were taken with a HITACHI HT7800 microscope. The hydrodynamic size (dynamic light scattering) of GPA-KLVFF-Gd was measured by Malvern Zetasizer (Nano-ZS90). HPLC curves were tested using Shimadzu Prominence LC-20A. The CD spectra curves of GPA-KLVFF-Gd before and after incubation with FAP were measured using a JASCO J-1500 spectropolarimeter. SEM images were taken with HITACHI Regulus 8100.

Molecular dynamics simulations

Molecular dynamics (MD) simulations of Gd-DOTA–modified peptides were conducted using GROMACS 2021.5 package. Peptides A (GTDTKTGPAKLVFFCKTDTG) and B (AKLVFFCKTDTG) were modeled using PEP-FOLD3. Peptides were parameterized by the Amberff14sb force field. A K residue (Lys) closest to the C terminus was modified by DOTA, and force field parameters and partial charges of modified K (MK) residue were modified from K residue in which the DOTA part was parameterized by Amberff14sb force field and was refitted by restrained electrostatic potential 2 (RESP2) charge. MK residue was geometrically optimized by Gaussian 16 under density functional theory B3LYP/def2-SVP level with DFT-D3 dispersion correction and SMD (water) implicit solvent model. Ambertools21 and ACPYPE were used to construct Amberff14sb force field parameters, Multiwfn was used to fit the RESP2 charge. Gd^{3+} was parameterized by the HFE parameter set for TIP3P water model developed by Li/Merz. MD simulation results were visualized by UCSF ChimeraX.

In vitro FAP response study

Three hundred microliters of GPA-KLVFF-Gd (0.19 mM) was mixed with different concentrations of FAP solution (4, 8, 12, 16, and 20 nM). Changes of size (TEM image), hydrodynamic size, relaxation time (T_1 and T_2), and in vitro MR imaging effect were measured. To determine the selectivity of GPA-KLVFF-Gd to FAP, ALP (1 mg/ml), GSH (1 mg/ml), H_2O_2 (1 mM), serum albumin (1 mg/ml), and FAP (20 nM) were added into 300 μl of GPA-KLVFF-Gd (0.19 mM). In vitro MR imaging images were recorded after coincubation for 6 hours.

In vitro MRI, longitudinal relaxivity (r_1), and transverse relaxivity (r_2)

T_1-weighted MRI images were acquired by a 1.0-T MR scanner (NIUMAG, NM42-060H-I). Scanning parameters were as follows: repetition time (TR)/echo time (TE) = 360 ms/18.14 ms, field of view (FOV) =60 mm × 60 mm, slice width = 2.5 mm, and slices = 4. Longitudinal time (T_1) and transverse relaxation time (T_2) of probes were measured by a 1.41-T MR analyzer (Minispec mq 60, Bruker, Germany) at 37°C. Linear fitting curves of Gd concentration (mM) versus $1/T_1$ (s^{-1}) and $1/T_2$ (s^{-1}) were drawn, respectively. The corresponding slope is longitudinal (r_1) and transverse relaxivity (r_2).

Cell activation, FAP expression, and FAP-catalyzed MRI enhancement in living cells

HSC-T6 cells were obtained from the Pricella Life Science & Technology Co. Ltd. FAP-negative HSC-T6 rat qHSCs can be activated by activators to become FAP-positive activated HSCs. HSC-T6 cells were serum starved for 12 hours before activation and then stimulated with TGF-β1 (5, 10, and 20 ng/ml) for 24 hours. The FAP expression of HSC-T6 cells was verified by anti-FAP immunofluorescence staining.

To verify the FAP-catalyzed MRI enhancement capability of the probe at the cellular level, HSC-T6 cells were seeded in six-well plates and activated for 24 hours. Then, the culture medium was replaced with fresh Dulbecco's modified Eagle's medium containing GPA-KLVFF-Gd (0.19 mM). After incubation for 12 hours, T_1-weighted MR phantom images of HSC-T6 cells with varying degrees of activation were obtained by a 1.0-T MR scanner.

BDL-induced liver fibrosis model establishment and in vivo T_1-weighted MRI

All animal experiments were approved by the TongJi hospital of TongJi University Animal Ethics Committee (no. 2024-DW-SB-208). Liver fibrosis was induced in male C57BL/6 mice by BDL surgery under anesthesia. The surgical area was meticulously disinfected with 75% alcohol to minimize infection risk. A midline abdominal incision exposed the liver, the bile duct was gently separated and identified using moistened sterile cotton swabs, then doubly ligated and transected to ensure complete obstruction. The abdominal cavity was closed layer by layer, and the skin was sutured.

To verify the probe's capability for early diagnosis and staging of liver fibrosis, healthy mice, mice 1 week postsurgery, and mice 2 weeks postsurgery were injected with 200 μl of GPA-KLVFF-Gd intravenously ($n \geq 3$ per group). Subsequently, T_1-weighted MR images at 3 min, 15 min, 30 min, 1 hour, 2 hours, 3 hours, 4 hours, and 6 hours postinjection were acquired. Mice injected with clinically used Magnevist or GAA-KLVFF-Gd were used as controls, and the

MR images of tumor were obtained at the same time points. In all in vivo MRI of this study, the amount of Gd^{3+} administered was 0.1 mmol/kg.

CCl_4-induced liver fibrosis model establishment and in vivo T_1-weighted MRI

Male Balb/c mice were intraperitoneally injected with CCl_4 twice a week to induce liver fibrosis (0.1 ml of 20% CCl_4 in olive oil the first week, 0.15 ml the second week, and 0.2 ml from weeks 3 to 12). To verify the probe's capability for liver fibrosis progression detection, healthy mice and mice continuously induced for 3, 5, and 10 weeks were intravenously injected with GPA-KLVFF-Gd, followed by MRI ($n \geq 3$ per group).

To investigate whether the probe can detect the fibrotic mice's response to treatment, after 10 weeks of continuous CCl_4 administration, treatment was administered using intraperitoneal injection of Res (10 mg/kg) twice a week. GPA-KLVFF-Gd was injected for MR imaging at 1 week and 3 weeks posttreatment.

In vivo MRI parameters and MRI data analysis

Scanning parameters in vivo were as follows: T_1-weighted sequence: TR/TE = 400 ms/18.14 ms, FOV = 60 mm × 60 mm, slice width = 2.5 mm, and slices = 12. Liver analysis was as follows: Three regions of interest (ROI) were manually traced (pixel number >100), encompassing the liver parenchyma while avoiding major blood vessels. Four ROIs (pixel number >100) were placed in the FOV without any tissue (air) to measure the variation in background signal. Bladder analysis was as follows: An ROI was manually traced (pixel number >100) encompassing the bladder. Four ROIs (pixel number >100) were placed in the FOV without any tissue (air) to measure the variation in background signal. The identical analysis was applied to images obtained before and after probe injection. Visualization and quantification of the images were performed using the Niumag NMR Image Processing Software version 3.0. The SNR and ΔSNR% were calculated using Eqs. 1 and 2

$$\mathrm{SNR} = \mathrm{SI}_{\mathrm{mean}} / \mathrm{SD}_{\mathrm{air}} \tag{1}$$

$$\Delta\mathrm{SNR}\% = \frac{\mathrm{SNR}_{\mathrm{after}} - \mathrm{SNR}_{\mathrm{before}}}{\mathrm{SNR}_{\mathrm{before}}} \times 100\% \tag{2}$$

Where SI_{mean} is the average signal intensity of the region of interest; SD_{air} is the SD of the signal in the air outside the animal, which was introduced with the aim of normalizing to eliminate systematic errors.

In vivo ultrasound imaging

Mice were subjected to BDL to induce liver fibrosis as previously described, and their livers were imaged at three different time points postoperatively: 3 days, 1 week, and 2 weeks. Ultrasound imaging was conducted using the multimodal small-animal ultrasound/photo-acoustic imaging system VEVO LAZR-X (Fujifilm VisualSonics) at a center frequency of 40 MHz.

Histology analysis

After imaging, animals were euthanized under anesthesia, and main organs were harvested. A piece of the left lobe of the liver was fixed with 4% paraformaldehyde, dehydrated, and embedded in paraffin. Tissue sections were stained with H&E, Sirius red, and subjected to immunofluorescence staining for α-SMA and FAP. The percentage of the area stained positive by SR, α-SMA, and FAP was measured with ImageJ.

In vivo biocompatibility evaluation of GPA-KLVFF-Gd

Balb/c mice were randomly assigned to two groups ($n = 3$). The first group received an intravenous injection of normal saline as a control, while the second group was injected with GPA-KLVFF-Gd. On the first day postinjection, blood was collected from mice by cardiac blood sampling for routine blood and biochemical analysis. Concurrently, animals were euthanized, and major organs (heart, liver, spleen, lungs, and kidneys) were harvested, fixed in 4% paraformaldehyde, and processed for H&E staining. The stained tissue sections were subsequently examined under an inverted microscope.

Statistical analysis

Data are presented as mean ± SD. Data comparisons were made using one-way and two-way analysis of variance (ANOVA). All statistical analyses were conducted using raw data or GraphPad Prism.

Supplementary Materials

This PDF file includes:

Figs. S1 to S15

REFERENCES AND NOTES

1. S. K. Asrani, H. Devarbhavi, J. Eaton, P. S. Kamath, Burden of liver diseases in the world. *J. Hepatol.* **70**, 151–171 (2019).
2. L. Xu, N. Wettschureck, Y. Bai, Z. Yuan, S. Wang, Myofibroblast YAP/TAZ is dispensable for liver fibrosis in mice. *J. Hepatol.* **75**, 238–241 (2021).
3. Q. Zhao, M.-Y. Dai, R.-Y. Huang, J.-Y. Duan, T. Zhang, W.-M. Bao, J.-Y. Zhang, S.-Q. Gui, S.-M. Xia, C.-T. Dai, Y.-M. Tang, F. J. Gonzalez, F. Li, Parabacteroides distasonis ameliorates hepatic fibrosis potentially via modulating intestinal bile acid metabolism and hepatocyte pyroptosis in male mice. *Nat. Commun.* **14**, 1829 (2023).
4. I. Mederacke, A. Filliol, S. Affo, A. Nair, C. Hernandez, Q. Sun, F. Hamberger, F. Brundu, Y. Chen, A. Ravichandra, P. Huebener, H. Anke, H. Shi, R. A. M. G. de la Torre, J. R. Smith, N. C. Henderson, F. W. R. Vondran, C. V. Rothlin, H. Baehre, I. Tabas, P. Sancho-Bru, R. F. Schwabe, The purinergic P2Y14 receptor links hepatocyte death to hepatic stellate cell activation and fibrogenesis in the liver. *Sci. Transl. Med.* **14**, eabe5795 (2022).
5. D. C. Rockey, S. L. Friedman, Fibrosis regression after eradication of hepatitis C virus: From bench to bedside. *Gastroenterology* **160**, 1502–1520.e1 (2021).
6. A. Maheux, Y. Purcell, S. Harguem, V. Vilgrain, M. Ronot, Targeted and non-targeted liver biopsies carry the same risk of complication. *Eur. Radiol.* **29**, 5772–5783 (2019).
7. M.-L. Kromrey, D. Le Bihan, S. Ichikawa, U. Motosugi, Diffusion-weighted MRI-based virtual elastography for the assessment of liver fibrosis. *Radiology* **295**, 127–135 (2020).
8. S. Robert, T. Gicquel, A. Bodin, A. Fautrel, E. Barreto, T. Victoni, V. Lagente, E. Boichot, Influence of inflammasome pathway activation in macrophages on the matrix metalloproteinase expression of human hepatic stellate cells. *Int. Immunopharmacol.* **72**, 12–20 (2019).
9. R. Loomba, L. A. Adams, Advances in non-invasive assessment of hepatic fibrosis. *Gut* **69**, 1343–1352 (2020).
10. T. C. Hollon, B. Pandian, A. R. Adapa, E. Urias, A. V. Save, S. S. S. Khalsa, D. G. Eichberg, R. S. D'Amico, Z. U. Farooq, S. Lewis, P. D. Petridis, T. Marie, A. H. Shah, H. J. L. Garton, C. O. Maher, J. A. Heth, E. L. McKean, S. E. Sullivan, S. L. Hervey-Jumper, P. G. Patil, B. G. Thompson, O. Sagher, G. M. McKhann, R. J. Komotar, M. E. Ivan, M. Snuderl, M. L. Otten, T. D. Johnson, M. B. Sisti, J. N. Bruce, K. M. Muraszko, J. Trautman, C. W. Freudiger, P. Canoll, H. Lee, S. Camelo-Piragua, D. A. Orringer, Near real-time intraoperative brain tumor diagnosis using stimulated Raman histology and deep neural networks. *Nat. Med.* **26**, 52–58 (2020).
11. K. Yamamoto, J. R. Brender, T. Seki, S. Kishimoto, N. Oshima, R. Choudhuri, S. S. Adler, E. M. Jagoda, K. Saito, N. Devasahayam, P. L. Choyke, J. B. Mitchell, M. C. Krishna, Molecular imaging of the tumor microenvironment reveals the relationship between tumor oxygenation, glucose uptake, and glycolysis in pancreatic ductal adenocarcinoma. *Cancer Res.* **80**, 2087–2093 (2020).
12. Z. Wu, W. Yang, B. Zhang, Enzyme-catalyzed molecular MR imaging of tumors. *TrAC Trends Anal. Chem.* **178**, 117848 (2024).

13. D. Liu, W. Yang, B. Zhang, Magnetic resonance imaging and its molecular probes in evaluating the response to tumor treatment. *Nano Biomed. Eng.* 10.26599/NBE.2024.9290073, (2024).
14. Z. Ding, H. Sun, S. Ge, Y. Cai, Y. Yuan, Z. Hai, T. Tao, J. Hu, B. Hu, J. Wang, G. Liang, Furin-controlled Fe_3O_4 nanoparticle aggregation and 19F signal "turn-on" for precise MR imaging of tumors. *Adv. Funct. Mater.* **29**, 1903860 (2019).
15. H. Du, Q. Wang, B. Zhang, Z. Liang, C. Huang, D. Shi, F. Li, D. Ling, Structural defect-enabled magnetic neutrality nanoprobes for ultra-high-field magnetic resonance imaging of isolated tumor cells in vivo. *Adv. Mater.* **36**, e2401538 (2024).
16. M. Pavlides, R. Banerjee, J. Sellwood, C. J. Kelly, M. D. Robson, J. C. Booth, J. Collier, S. Neubauer, E. Barnes, Multiparametric magnetic resonance imaging predicts clinical outcomes in patients with chronic liver disease. *J. Hepatol.* **64**, 308–315 (2016).
17. T. Allkemper, F. Sagmeister, V. Cicinnati, S. Beckebaum, H. Kooijman, C. Kanthak, C. Stehling, W. Heindel, Evaluation of fibrotic liver disease with whole-liver T1ρ MR imaging: A feasibility study at 1.5 T. *Radiology* **271**, 408–415 (2014).
18. K. J. Glaser, A. Manduca, R. L. Ehman, Review of MR elastography applications and recent developments. *J. Magn. Reson. Imaging* **36**, 757–774 (2012).
19. S. Li, X. Sun, M. Chen, Z. Ying, Y. Wan, L. Pi, B. Ren, Q. Cao, Liver fibrosis conventional and molecular imaging diagnosis update. *J. Liver* **08**, 236 (2019).
20. S. B. Montesi, P. Désogère, B. C. Fuchs, P. Caravan, Molecular imaging of fibrosis: Recent advances and future directions. *J. Clin. Invest.* **129**, 24–33 (2019).
21. K. J. Fowler, M. R. Bashir, The current status of imaging in liver fibrosis. *Nat. Rev. Gastroenterol. Hepatol.* **20**, 628–629 (2023).
22. B. C. Fuchs, H. Wang, Y. Yang, L. Wei, M. Polasek, D. T. Schühle, G. Y. Lauwers, A. Parkar, A. J. Sinskey, K. K. Tanabe, P. Caravan, Molecular MRI of collagen to diagnose and stage liver fibrosis. *J. Hepatol.* **59**, 992–998 (2013).
23. C. T. Farrar, D. K. DePeralta, H. Day, T. A. Rietz, L. Wei, G. Y. Lauwers, B. Keil, A. Subramaniam, A. J. Sinskey, K. K. Tanabe, B. C. Fuchs, P. Caravan, 3D molecular MR imaging of liver fibrosis and response to rapamycin therapy in a bile duct ligation rat model. *J. Hepatol.* **63**, 689–696 (2015).
24. B. Zhu, L. Wei, N. Rotile, H. Day, T. Rietz, C. T. Farrar, G. Y. Lauwers, K. K. Tanabe, B. Rosen, B. C. Fuchs, P. Caravan, Combined magnetic resonance elastography and collagen molecular magnetic resonance imaging accurately stage liver fibrosis in a rat model. *Hepatol. Baltim. Md* **65**, 1015–1025 (2017).
25. I. Y. Zhou, V. Clavijo Jordan, N. J. Rotile, E. Akam, S. Krishnan, G. Arora, H. Krishnan, H. Slattery, N. Warner, N. Mercaldo, C. T. Farrar, J. Wellen, R. Martinez, F. Schlerman, K. K. Tanabe, B. C. Fuchs, P. Caravan, Advanced MRI of liver fibrosis and treatment response in a rat model of nonalcoholic steatohepatitis. *Radiology* **296**, 67–75 (2020).
26. J. Gao, Y. Wang, X. Meng, X. Wang, F. Han, H. Xing, G. Lv, L. Zhang, S. Wu, X. Jiang, Z. Yao, X. Fang, J. Zhang, W. Bu, A FAPα-activated MRI nanoprobe for precise grading diagnosis of clinical liver fibrosis. *Nat. Commun.* **15**, 8036 (2024).
27. J. Kim, Y. Eygeris, R. C. Ryals, A. Jozić, G. Sahay, Strategies for non-viral vectors targeting organs beyond the liver. *Nat. Nanotechnol.* **19**, 428–447 (2024).
28. S. Yazdani, R. Bansal, J. Prakash, Drug targeting to myofibroblasts: Implications for fibrosis and cancer. *Adv. Drug Deliv. Rev.* **121**, 101–116 (2017).
29. T. Kisseleva, D. Brenner, Molecular and cellular mechanisms of liver fibrosis and its regression. *Nat. Rev. Gastroenterol. Hepatol.* **18**, 151–166 (2021).
30. M. Qi, S. Fan, M. Huang, J. Pan, Y. Li, Q. Miao, W. Lyu, X. Li, L. Deng, S. Qiu, T. Liu, W. Deng, X. Chu, C. Jiang, W. He, L. Xia, Y. Yang, J. Hong, Q. Qi, W. Yin, X. Liu, C. Shi, M. Chen, W. Ye, D. Zhang, Targeting FAPα-expressing hepatic stellate cells overcomes resistance to antiangiogenics in colorectal cancer liver metastasis models. *J. Clin. Invest.* **133**, e168771 (2022).
31. J. Wahsner, E. M. Gale, A. Rodríguez-Rodríguez, P. Caravan, Chemistry of MRI contrast agents: Current challenges and new frontiers. *Chem. Rev.* **119**, 957–1057 (2019).
32. E. Arad, H. Green, R. Jelinek, H. Rapaport, Revisiting thioflavin T (ThT) fluorescence as a marker of protein fibrillation – The prominent role of electrostatic interactions. *J. Colloid Interface Sci.* **573**, 87–95 (2020).
33. N. Bloembergen, Spin relaxation processes in a two-proton system. *Phys. Rev.* **104**, 1542–1547 (1956).
34. I. Solomon, N. Bloembergen, Nuclear magnetic interactions in the HF molecule. *J. Chem. Phys.* **25**, 261–266 (1956).
35. N. Bloembergen, Proton relaxation times in paramagnetic solutions. *J. Chem. Phys.* **27**, 572–573 (1957).
36. N. Bloembergen, L. O. Morgan, Proton relaxation times in paramagnetic solutions. Effects of electron spin relaxation. *J. Chem. Phys.* **34**, 842–850 (1961).
37. Z. Deng, T. Fan, C. Xiao, H. Tian, Y. Zheng, C. Li, J. He, TGF-β signaling in health, disease, and therapeutics. *Signal Transduct. Target. Ther.* **9**, 61 (2024).
38. P. Santiago, A. R. Scheinberg, C. Levy, Cholestatic liver diseases: New targets, new therapies. *Therap. Adv. Gastroenterol.* **11**, 1756284818787400 (2018).
39. K. Ishak, A. Baptista, L. Bianchi, F. Callea, J. De Groote, F. Gudat, H. Denk, V. Desmet, G. Korb, R. N. MacSween, Histological grading and staging of chronic hepatitis. *J. Hepatol.* **22**, 696–699 (1995).
40. Z. D. Goodman, Grading and staging systems for inflammation and fibrosis in chronic liver diseases. *J. Hepatol.* **47**, 598–607 (2007).
41. J. Garcia-Pardo, S. Ventura, Chemical targeting of amyloids. *Nat. Chem. Biol.* **19**, 1176–1177 (2023).
42. H.-W. An, L.-L. Li, Y. Wang, Z. Wang, D. Hou, Y.-X. Lin, S.-L. Qiao, M.-D. Wang, C. Yang, Y. Cong, Y. Ma, X.-X. Zhao, Q. Cai, W.-T. Chen, C.-Q. Lu, W. Xu, H. Wang, Y. Zhao, A tumour-selective cascade activatable self-detained system for drug delivery and cancer imaging. *Nat. Commun.* **10**, 4861 (2019).
43. D. Scholten, J. Trebicka, C. Liedtke, R. Weiskirchen, The carbon tetrachloride model in mice. *Lab. Anim.* **49**, 4–11 (2015).
44. Y. Hao, K. Song, X. Tan, L. Ren, X. Guo, C. Zhou, H. Li, J. Wen, Y. Meng, M. Lin, Y. Zhang, H. Huang, L. Wang, W. Zheng, Reactive oxygen species-responsive polypeptide drug delivery system targeted activated hepatic stellate cells to ameliorate liver fibrosis. *ACS Nano* **16**, 20739–20757 (2022).
45. Y. L. Balachandran, W. Wang, H. Yang, H. Tong, L. Wang, F. Liu, H. Chen, K. Zhong, Y. Liu, X. Jiang, Heterogeneous iron oxide/dysprosium oxide nanoparticles target liver for precise magnetic resonance imaging of liver fibrosis. *ACS Nano* **16**, 5647–5659 (2022).
46. Y. Ning, I. Y. Zhou, J. D. Roberts Jr., N. J. Rotile, E. Akam, S. C. Barrett, M. Sojoodi, M. N. Barr, T. Punshon, P. Pantazopoulos, H. K. Drescher, B. P. Jackson, K. K. Tanabe, P. Caravan, Molecular MRI quantification of extracellular aldehyde pairs for early detection of liver fibrogenesis and response to treatment. *Sci. Transl. Med.* **14**, eabq6297 (2022).
47. M. Salarian, R. C. Turaga, S. Xue, M. Nezafati, K. Hekmatyar, J. Qiao, Y. Zhang, S. Tan, O. Y. Ibhagui, Y. Hai, J. Li, R. Mukkavilli, M. Sharma, P. Mittal, X. Min, S. Keilholz, L. Yu, G. Qin, A. B. Farris, Z.-R. Liu, J. J. Yang, Early detection and staging of chronic liver diseases with a protein MRI contrast agent. *Nat. Commun.* **10**, 4777 (2019).
48. H.-W. Liu, L. Chen, C. Xu, Z. Li, H. Zhang, X.-B. Zhang, W. Tan, Recent progresses in small-molecule enzymatic fluorescent probes for cancer imaging. *Chem. Soc. Rev.* **47**, 7140–7180 (2018).
49. Y. Hu, J. Zhang, Y. Miao, X. Wen, J. Wang, Y. Sun, Y. Chen, J. Lin, L. Qiu, K. Guo, H.-Y. Chen, D. Ye, Enzyme-mediated in situ self-assembly promotes in vivo bioorthogonal reaction for pretargeted multimodality imaging. *Angew. Chem. Int. Ed. Engl.* **60**, 18082–18093 (2021).
50. X. Ma, X. Liang, M. Yao, Y. Gao, Q. Luo, X. Li, Y. Yu, Y. Sun, M. H. Y. Cheng, J. Chen, G. Zheng, J. Shi, F. Wang, Myoglobin-loaded gadolinium nanotexaphyrins for oxygen synergy and imaging-guided radiosensitization therapy. *Nat. Commun.* **14**, 6187 (2023).
51. Z. Ma, K. Lin, M. Tang, M. Ramachandran, R. Qiu, J. Li, L. N. Solano, Y. Huang, C. De Souza, S. Abou-Adas, B. Xiang, L. Zhang, M. Li, Y. Li, A pH-driven small-molecule nanotransformer hijacks lysosomes and overcomes autophagy-induced resistance in cancer. *Angew. Chem. Int. Ed. Engl.* **61**, e202204567 (2022).

Acknowledgments: The liver pattern and cell pattern in Fig. 1B were created using BioRender.com. **Funding:** This work was supported by National Natural Science Foundation of China (82272055, B.Z.; and 82272137, W.Y.), National Key Research and Development Project (2022YFB3804500, B.Z.), Program of Shanghai Municipal Health Commission (20224Y0013, Y.X.), and China Postdoctoral Science Foundation (2023M732656, Y.X.). **Author contributions:** Conceptualization: Z.W., W.Y., B.Z., K.B., D.L., and C.L. Methodology: Z.W., B.Z., H.W., W.Y., and D.L. Investigation: Z.W., B.Z., W.Y., K.B., D.L., J.Y., and Y.X. Visualization: Z.W., B.Z., D.L., and W.Z. Supervision: W.Y., B.Z., and Z.W. Resources: Z.W., B.Z., W.Y., and C.L. Funding acquisition: B.Z. and Y.X. Data curation: B.Z., W.Y., C.L., and Z.W. Validation: B.Z., W.Y., K.B., D.L., W.Z., C.L., Y.X., and Z.W. Formal analysis: B.Z., W.Y., J.Y., and Z.W. Software: B.Z., W.Y., Z.W. Project administration: B.Z., W.Y., and Z.W. Writing–original draft: Z.W., Writing–review and editing: Z.W., W.Y., B.Z., K.B., D.L., C.L., and Y.X. **Competing interests:** The authors declare that they have no competing interests. **Data and materials availability:** All data needed to evaluate the conclusions in the paper are present in the paper and/or the Supplementary Materials.

Submitted 4 October 2024
Accepted 4 February 2025
Published 12 March 2025
10.1126/sciadv.adt6082